CAUCHY – Jurnal Matematika Murni dan Aplikasi
Volume 11 (1) (2026), Pages 16-31
p-ISSN: 2086-0382; e-ISSN: 2477-3344

# Interpolation of Fire Radiative Power Based on GSTAR Model Predictions with Queen Contiguity Weights Using Ordinary Kriging

Gita Fitriyana[1], Nurfitri Imro'ah[1*], and Nur'ainul Miftahul Huda[2]

[1]*Department of Statistics, Faculty of Mathematics and Natural Sciences, Universitas Tanjungpura, Pontianak, Indonesia*
[2]*Department of Mathematics, Faculty of Mathematics and Natural Sciences, Universitas Tanjungpura, Pontianak, Indonesia*

**Abstract**

Forest fires are a persistent environmental issue in West Kalimantan, Indonesia, driven by both natural and human factors. Fire Radiative Power (FRP) serves as a vital indicator for assessing wildfire intensity and energy release. This study aims to model and predict the spatial temporal dynamics of FRP using the Generalized Space Time Autoregressive [GSTAR(1;1)] model combined with Ordinary Kriging interpolation. The dataset covers West Kalimantan from July 2024 to September 2025, comprising four attributes: observation date, longitude, latitude, and FRP value. Data filtering was applied from the national to provincial level, focusing on three regencies Sanggau, Sekadau, and Ketapang across 14 sub-districts represented by a $1.25 \times 1.25$ grid. The data consisted of 65 weekly observations, with 61 used for training and 4 for testing. The GSTAR(1;1) model with a spatial area-based framework achieved an optimal RMSE of 7.42 and satisfied the white noise assumption, indicating reliable performance. Predictions for October 2025 indicated relatively stable fire intensity, with a slight FRP decrease in Nanga Tayap and Sandai during the final week. Overall, the integrated GSTAR–Kriging framework effectively captured both temporal and spatial variations, supporting improved fire risk assessment and regional decision making for wildfire management in West Kalimantan.

**Keywords:** Weight; Spatial Temporal; Kriging; Forest Fire.



## 1. Introduction

Fire Radiative Power (FRP) serves as a fundamental indicator for characterising fire behaviour, as it reflects the rate at which heat energy is released during combustion [1]. In addition, FRP functions as an important parameter for assessing wildfire intensity, providing more detailed quantitative information than conventional fire perimeter or burned area datasets that typically offer only binary classifications [2]. Furthermore, FRP represents a valuable quantitative indicator of fire activity and its temporal variations over the study period [3]. Over the past two decades, numerous operational remote sensing approaches have been developed and widely implemented to estimate FRP, enabling the evaluation of combustion intensity and emission levels [4]. Therefore,

[*]**Corresponding author**. E-mail: nurfitriimroah@math.untan.ac.id

Submitted: November 12, 2025 Reviewed: November 22, 2025 Accepted: December 07, 2025
DOI: https://doi.org/10.18860/cauchy.v11i1.37462

accurate prediction of FRP is essential not only for improving the effectiveness of wildfire management and suppression strategies but also for assessing the environmental pollution impacts arising from such events [5].

Forest fires are among the most frequent environmental disasters in Indonesia, particularly in the province of West Kalimantan. These events are driven by a combination of natural factors, such as prolonged droughts and the El Niño phenomenon, alongside human activities like land clearing through burning practices [6]. Additionally, forest fires also referred to as bushfires or vegetation fires can be triggered by climatic shifts that are further intensified by increasing greenhouse gas emissions and global warming [7]. In fact, more than 90% of forest fires are attributed to human activities, while the remaining cases are primarily caused by natural phenomena such as lightning strikes [8]. In this study, the analysis focuses on three regencies: Sanggau, Sekadau, and Ketapang, which collectively represent the primary hotspot corridor in West Kalimantan (see Fig. 1a). Fig. 1b classifies the regencies based on their total accumulated FRP, with colors indicating the ranking: Red (highest), Pink (moderate), and Yellow (lower). Ketapang (319.1 MW) and Sanggau (279.2 MW) record the highest peak FRP intensities, whereas Sekadau (199.0 MW), despite a lower maximum value, was included because it geographically connects the two major hotspot regions. These three regencies thus form a spatially contiguous zone of intense fire activity extending from the central region to the southern coast, making them suitable for spatial temporal interaction analysis.

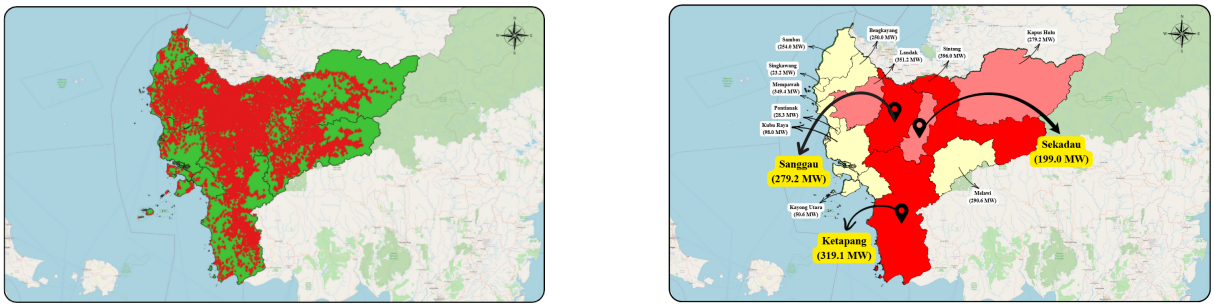


**(a)** **(b)**

**Fig. 1:** Spatial distribution of FRP in (a) West Kalimantan and (b) the selected study area comprising Sanggau, Sekadau, and Ketapang regencies.

To analyze the spatial and temporal dynamics of fire activity in the study area, this research employs the Generalized Space–Time Autoregressive (GSTAR) model with a spatial weight matrix based on the Queen contiguity criterion. The GSTAR(1;1) specification is particularly suitable for modelling the interdependence of fire behaviour across neighbouring regions over time, allowing the identification of spatial autocorrelation and temporal persistence in FRP values, since the GSTAR model explains the manner in which patterns of change and interactions occur between locations within a spatial-temporal system [9]. By incorporating both spatial and temporal components, this model can effectively capture the propagation patterns of fire activity between adjacent grid areas [10]. The best-performing GSTAR model is then used to generate FRP predictions, which are subsequently interpolated using the Ordinary Kriging technique. This method is recognised as the most effective linear and unbiased interpolation for estimating unknown spatial values [11] and provides a geostatistical framework for estimating FRP intensity at unsampled locations and enhancing spatial continuity. The integration of GSTAR and Ordinary Kriging enables a comprehensive spatial-temporal assessment, revealing not only how fire activity evolves over time but also how it spreads spatially across West Kalimantan.

Several previous studies have explored FRP prediction using spatial approaches. A study combining the GSTAR and Ordinary Kriging models analyzed $CO_2$ emission variability in Asia, identifying China, India, and Indonesia as the largest contributors. The GSTAR(3;1,1,1) model provided optimal forecasts with low RMSE and MAPE values, while the isotropic spherical

semivariogram in Kriging produced accurate spatial predictions, indicating persistently high emissions in northeastern Asia until 2027 [12]. Another study utilizing FRP data from MODIS satellites across countries such as Nepal, Bhutan, and Sri Lanka applied spatial statistical methods including the Spatial Lag Model, Spatial Error Model, and Kriging to map and predict FRP distribution. Kriging interpolation was used to estimate fire potential in unobserved areas, offering a comprehensive overview of fire risk and impact [13]. Additionally, a study on peatland fires in Kubu Raya Regency, West Kalimantan, analyzed fire dynamics using temporal, spatial, and spatial temporal approaches. The ARIMA model captured temporal trends, Kriging interpolation mapped spatial hotspot distribution, and the GSTAR model identified areas with a high potential for future fire spread [14].

This study aims to model and predict the spatial-temporal dynamics of FRP across 14 selected sub-districts within the regencies of Sanggau, Sekadau, and Ketapang in West Kalimantan Province using the GSTAR model combined with the Ordinary Kriging method. The main objective is to capture both the spatial interaction and temporal persistence of fire activity, enabling a more detailed understanding of fire propagation patterns within the study area. By integrating FRP with geostatistical and spatial-temporal modelling techniques, this research aims to produce accurate and continuous predictions of fire intensity distribution. The novelty of this study lies in combining GSTAR for temporal forecasting and Ordinary Kriging for spatial interpolation, providing a robust framework to improve fire risk assessment and support regional decision-making for wildfire management and environmental protection in West Kalimantan.

## 2. Methods

This study adopts a quantitative research approach that integrates spatial and temporal analysis through the GSTAR model. The objective is to analyse and model the spatial-temporal dynamics of FRP across selected sub-districts in Sanggau, Sekadau, and Ketapang Regencies, West Kalimantan. The best GSTAR model results are further refined using the Ordinary Kriging method to generate spatially continuous predictions of fire intensity.

### 2.1. Generalized Space-Time Autoregressive Model (GSTAR)

The Generalized Space-Time Autoregressive (GSTAR) model is commonly applied in conducting spatio-temporal analysis [15]. The autoregressive (AR) model served as the foundation for the development of the space-time autoregressive (STAR) model, which later evolved into the generalized spatio-temporal autoregressive (GSTAR) model that extends its predecessors by incorporating both spatial interactions among locations and temporal variations over time [6, 16]. The GSTAR model can be represented as follows.

$$\mathbf{Y}_t = \sum_{s=1}^{p} \left[ \mathbf{\Phi}_{s0} + \sum_{k=1}^{\lambda_s} \mathbf{\Phi}_{sk} \mathbf{W}_k \right] \mathbf{Y}_{t-k} + \mathbf{e}_t$$

where $\mathbf{W}_k$ is weight matrix. Assuming that $\mathbf{Y}_t$ follows the GSTAR(1;1) model, then:

$$\mathbf{Y}_t = \mathbf{\Phi}_{10} \mathbf{W}^{(0)} \mathbf{Y}_{t-1} + \mathbf{\Phi}_{11} \mathbf{W}^{(1)} \mathbf{Y}_{t-1} + \mathbf{e}_t$$

where,

$$\begin{aligned}
\mathbf{Y}_t &= \begin{bmatrix} Y_t^{(1)} & Y_t^{(2)} & \dots & Y_t^{(N)} \end{bmatrix}^t \\
\mathbf{\Phi}_{10} &= \text{diag}(\phi_{10}^{(1)}, \phi_{10}^{(2)}, \dots, \phi_{10}^{(N)}) \\
\mathbf{\Phi}_{11} &= \text{diag}(\phi_{11}^{(1)}, \phi_{11}^{(2)}, \dots, \phi_{11}^{(N)}) \\
\mathbf{e}_t &= \begin{bmatrix} e_t^{(1)} & e_t^{(2)} & \dots & e_t^{(N)} \end{bmatrix}^t
\end{aligned}$$

The variables in the model are defined as follows: $\mathbf{Y}_t$ is observations in period $t$, while $\mathbf{Y}_{t-1}$ is observations in the preceding period, $t-1$. The parameter $\mathbf{\Phi}_{10}$ is the autoregressive coefficient for the influence of the location itself, whereas $\mathbf{\Phi}_{11}$ is the autoregressive coefficient for the influence of neighboring locations. Furthermore, $\mathbf{W}^{(0)}$ is an identity matrix, $\mathbf{W}^{(1)}$ is the spatial weight matrix, and $\mathbf{e}_t$ is the error term in period $t$.

## 2.2. Queen Contiguity Weight Matrix

The spatial weight matrix plays a crucial role in constructing the GSTAR model, as it helps represent the spatial relationships among different locations [17]. It also serves as a fundamental element in spatial analysis, providing a means to evaluate the interactions and dependencies that occur among geographic areas [18]. A spatial weight matrix can be built in several ways, one of which is the queen contiguity method. In this method, the weight of each location is based on nearby areas that share common boundaries or corner points [16]. The spatial weight matrix must satisfy specific conditions. A primary requirement is that a location has no spatial influence on itself, meaning the diagonal elements of the matrix are zero ($w_{ij} = 0$ for $i = j$, where $i = 1, 2, \ldots, N$). Therefore, the general form of the $N \times N$ weight matrix, denoted as $\mathbf{W}$, can be represented as follows [19]:

$$\mathbf{W}^{(\ell)} = \begin{bmatrix} 0 & w_{12}^{(\ell)} & \ldots & w_{1N}^{(\ell)} \\ w_{21}^{(\ell)} & 0 & \ldots & w_{2N}^{(\ell)} \\ \vdots & \vdots & \ddots & \vdots \\ w_{N1}^{(\ell)} & w_{N2}^{(\ell)} & \ldots & 0 \end{bmatrix}$$

where $\mathbf{W}^{(\ell)}$ represents the spatial weight matrix at spatial lag $\ell$.

## 2.3. Ordinary Kriging

Kriging is a geostatistical technique used to perform spatial interpolation [20]. It encompasses a set of interpolation methods grounded in geostatistics that aim to provide unbiased estimates of variable values across a surface [21]. In general, various types of kriging methods are available, including ordinary, simple, universal, Poisson probability, and others [22]. Among these, Ordinary Kriging is recognized as an effective and efficient approach for interpolating sparse geospatial data across extensive areas [20]. This method utilizes spatial data from sampled points along with variograms that describe the correlation between spatial locations to estimate values at unsampled sites, where the predicted values are influenced by their proximity to the sampled locations [23]. This method assumes that the study variable at any given location is a stationary random function, meaning that its mean value remains constant throughout the study area, although the exact value of the mean is unknown [24]. The equation of the Ordinary Kriging model is expressed as follows [25].

$$\hat{Z}(u_i) = \sum_{i=1}^{n} w_i Z(u_i)$$

where the value at an unobserved location, $u_i$, is estimated and denoted by $\hat{Z}(u_i)$. This estimate is calculated as a weighted average of the observed values, $Z(u_i)$, from $n$ surrounding data points at locations $u_i$. Each of these observations is assigned a specific weight, $w_i$, which is determined by the distance and spatial relationship between the points. One of the main objectives of the Kriging method is to obtain an optimal, linear, and unbiased estimate (BLUE) [26].

## 2.4. Variogram and Semivariogram

The variogram is a key instrument in geostatistics that illustrates the spatial autocorrelation and measurement variability among the data points being analyzed [20], and it plays a crucial

role in determining the weighting factors used for interpolation in the Kriging process [24]. The estimated experimental variogram can be expressed as follows [23]:

$$2\hat{\gamma}(h) \equiv \frac{1}{|N(h)|} \sum_{N(h)} [z(s_i) - z(s_j)]^2$$

where $z(s_i)$ and $z(s_j)$ are field values at locations $s_i$ and $s_j$, respectively. The set of all location pairs separated by the lag distance **h** is denoted by $N(h) = \{(s_i, s_j) : s_i - s_j \in h \text{ for } i, j = 1, \ldots, N\}$, whereas $|N(h)|$ denotes the number of distinct pairs in $N(h)$.

The semivariogram is defined as one-half of the variogram value [2]. In general, semivariograms are categorized into two types: the empirical semivariogram and the theoretical semivariogram [23]. The experimental semivariogram represents a plot of semivariance values $\gamma(h)$ as a function of the separation distance $h$ [27]. The experimental semivariogram is derived from observed or sampled data using the following equation [28].

$$\hat{\gamma}(h) \equiv \frac{1}{2|N(h)|} \sum_{N(h)} [z(s_i) - z(s_j)]^2$$

The experimental semivariogram values are subsequently compared with theoretical models to determine the best-fitting one, which is then used in calculating the weights for the Kriging interpolation process. In general, theoretical semivariograms are classified into three main types: Spherical, Exponential, and Gaussian [29].

The research workflow is presented in Fig. 2, outlining the sequential procedures carried out in this study from data acquisition and preprocessing to model development, validation, and spatial interpolation using the GSTAR–Kriging approach.

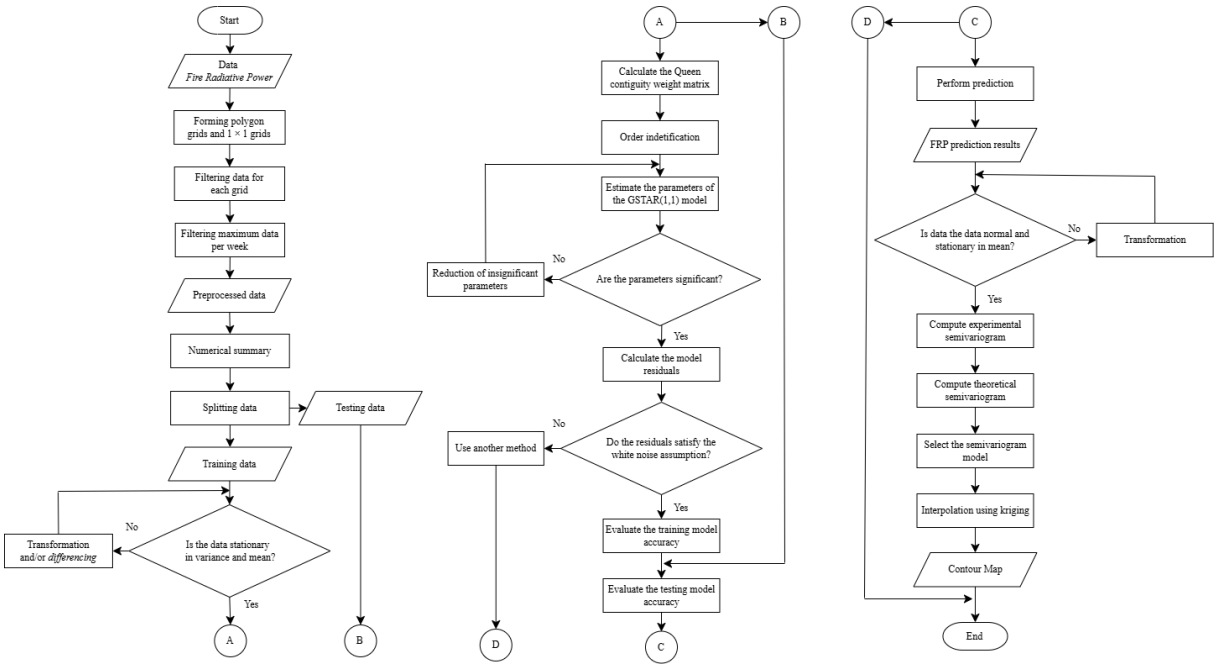


**Fig. 2:** Research flowchart

## 3. Results and Discussion

The data used in this study comprise Fire Radiative Power (FRP) values obtained from the VIIRS NOAA-20 satellite through the official NASA FIRMS platform. FRP represents the rate of radiant energy released by active fires, expressed in megawatts (MW), and serves as an indicator of fire intensity and combustion efficiency. An illustration of the FRP data distribution can be seen in Fig. 3 [30].

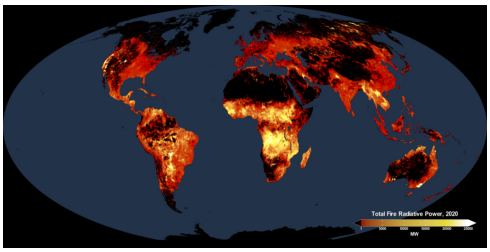


**Fig. 3:** Ilustration of Fire Radiative Power

The dataset covers West Kalimantan Province over the period from July 2024 to September 2025 and includes four key attributes: observation date, longitude, latitude, and FRP value. The initial stage of data processing involved applying a geographical filter, starting from the national scale (covering all of Indonesia), which was then narrowed to Kalimantan Island and further refined to West Kalimantan Province specifically focusing on three regencies: Sanggau, Sekadau, and Ketapang. From these regencies, 14 sub-districts were selected as the spatial units of analysis (see Fig. 4a).

Subsequently, the 14 sub-districts were transformed into spatial representations using $1.25 \times 1.25$ grid, resulting in three research zones labeled A1, A2, and A3 (see Fig. 4b). Following the spatial transformation, data preprocessing was carried out to ensure the dataset met the assumptions required for model development. The FRP data were aggregated into 65 weekly observations, with each observation representing the maximum FRP value recorded during that week for each grid area. From this dataset, 61 observations (July 2024–August 2025) were used as the training set, while the remaining 4 observations (September 2025) served as the testing set. The trained model was then used to generate predictions for October 2025.

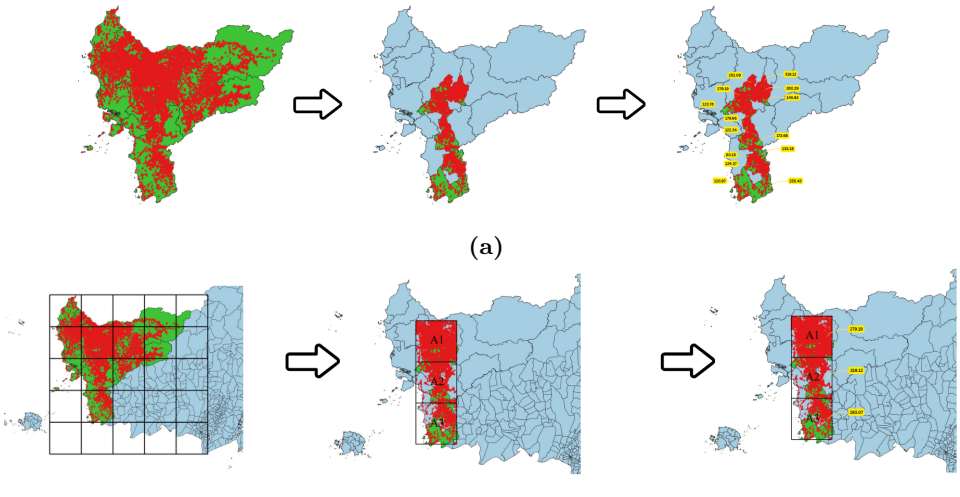


**(a)**

**(b)**

**Fig. 4:** Illustration of the data preprocessing process for (a) spatial area-based and (b) $1.25 \times 1.25$ grid cells.

To visually examine the temporal dynamics and characteristics of the prepared data, time series plot of the weekly maximum FRP values are presented in Fig. 5. The figure illustrates the data from two perspectives: the spatial area-based (administrative sub-districts) units that serve as the direct input for the GSTAR model, and the $1.25 \times 1.25$ grid cells, which provide a visual and contextual comparison.

A visual examination of the plots reveals a distinct seasonal pattern in fire activity across the study area. The time series at both the district level (see Fig. 5a) and the grid-based representation (see Fig. 5b) exhibit two prominent peaks, occurring approximately around weeks 11–13 and week 56, which coincide with the dry season when fires are most prevalent. In Fig. 5a,

only a subset of representative districts three selected areas is displayed to illustrate the general temporal trend observed across all regions. After spatial aggregation into grid form, this temporal pattern remains evident and demonstrates strong synchronization among locations, indicating the presence of spatial dependence in fire occurrences, which provides the key rationale for applying the GSTAR model.

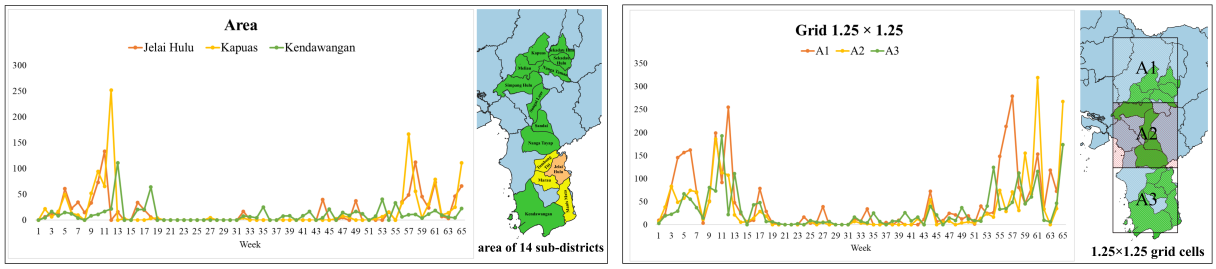


**(a)** **(b)**

**Fig. 5:** FRP data plot and ilustration of Queen Contiguity weight for (a) spatial area-based and (b) $1.25 \times 1.25$ grid cells.

While these plots effectively illustrate the temporal dynamics and spatial co-movement of fire activity, a more formal quantitative summary is necessary to compare the statistical characteristics of each location accurately. Therefore, a descriptive statistical analysis was conducted, and the results are summarized in Table 1.

**Table 1:** Statistical summary. The bolded numbers represents the maximum values.

| Spatial Unit | Locations ($i$) | Maximum | Minimum | Mean | Std. Deviation |
|---|---|---|---|---|---|
| Area | Jelai Hulu (1) | 133.18 | 0.51 | 16.22 | 27.73 |
| | Kapuas (2) | 252.09 | 2.66 | 18.05 | 42.37 |
| | Kendawangan (3) | 110.97 | 3.86 | 10.55 | 16.98 |
| | Manis Mata (4) | 193.07 | 2.33 | 10.21 | 26.81 |
| | Marau (5) | 173.68 | 1.16 | 14.17 | 31.67 |
| | Meliau (6) | 279.19 | 3.28 | **25.41** | **49.03** |
| | Nanga Taman (7) | 145.93 | 3.13 | 14.32 | 31.03 |
| | Nanga Tayap (8) | 107.59 | 2.54 | 10.71 | 20.79 |
| | Sandai (9) | 255.43 | 3.23 | 19.01 | 42.36 |
| | Sekadau Hilir (10) | 182.54 | 3.66 | 13.37 | 30.52 |
| | Sekadau Hulu (11) | 198.95 | 2.35 | 16.13 | 36.51 |
| | Simpang Hulu (12) | **319.12** | 2.31 | 17.52 | 47.28 |
| | Sungai Laur (13) | 280.29 | 2.59 | 17.58 | 47.13 |
| | Tumbang Titi (14) | 82.48 | 0.91 | 8.48 | 16.99 |
| Grid $1.25 \times 1.25$ | A1 (1) | 279.19 | 0.48 | **50.05** | **67.91** |
| | A2 (2) | **319.12** | 2.26 | 33.89 | 60.60 |
| | A3 (3) | 193.07 | 2.37 | 31.18 | 40.95 |

*Note: All FRP values are expressed in Megawatts (MW).*

Based on Table 1, the analysis at the polygon (sub-district) level shows clear variations in fire intensity across regions. The highest maximum FRP values are observed in Simpang Hulu (319.12 MW) and Sungai Laur (280.29 MW), which occurred during week 61, corresponding to August 2025, indicating that the most intense fire events took place in these sub-districts. Regarding the average FRP, Meliau (25.41 MW) records the highest value within the past year, suggesting that this area consistently experienced elevated fire activity compared to other sub-districts such as Marau (14.17 MW) and Tumbang Titi (8.48 MW). The relatively high standard deviations observed in Meliau (49.03) and Simpang Hulu (47.28) further indicate fluctuating fire intensity patterns characterized by intermittent peaks of extreme fire activity.

When the data are aggregated into the $1.25 \times 1.25$ grid system, which serves as the direct input for the GSTAR model, a clearer picture of the broader hotspot zones emerges. A key observation is that Grid A1 exhibits the highest mean FRP value (50.05 MW), substantially exceeding that of Grid A2 (33.89 MW) and Grid A3 (31.18 MW). This indicates that Grid A1 consistently experienced higher fire intensity throughout the past year of observation.

Conversely, the most extreme single event occurred within Grid A2, which recorded a maximum FRP of 319.12 MW. This peak was observed in week 61, corresponding to August 2025, and directly aligns with the highest FRP detected in the Sekadau Hilir sub-district, confirming that this major fire event was geographically located within the A2 grid boundaries. The relatively high standard deviations in Grid A1 (67.91) and Grid A2 (60.60) further reinforce the visual findings from the plots, suggesting that these two grids are not only the most active but also the most volatile areas.

### 3.1. Stasionarity Test

In constructing the GSTAR model, it is essential to ensure that the data exhibit stability in both their mean and variance [31]. To evaluate mean stationarity, the Augmented Dickey-Fuller (ADF) test was first applied to the original (non-differenced) series [32]. The initial ADF results showed that several locations exhibited p-values greater than 0.05, indicating non-stationarity in mean. Therefore, differencing was performed on these series. Table 2 presents the ADF results after differencing, which show that the transformed series have become stationary, with p-values below 0.05 for all but one location.

**Table 2:** ADF Test Results

| **ADF Test** | **Locations ($i$)** | | | | | | | | | | | | | |
|---|---|---|---|---|---|---|---|---|---|---|---|---|---|---|
| | **1** | **2** | **3** | **4** | **5** | **6** | **7** | **8** | **9** | **10** | **11** | **12** | **13** | **14** |
| Area | 0.01 | 0.01 | 0.01 | 0.01 | 0.01 | 0.01 | 0.01 | 0.01 | 0.01 | 0.01 | 0.01 | 0.18 | 0.04 | 0.01 |
| Grid 1.25×1.25 | 0.01 | 0.04 | 0.01 | | | | | | | | | | | |

### 3.2. Queen Contiguity Weight Matrix

The Queen Contiguity rule will be applied in the next step to construct the spatial weight matrix. By implementing this rule on the generated location, two matrices are defined as $\boldsymbol{W}_{Q1}^{(1)}$ for the spatial area-based model and $\boldsymbol{W}_{Q2}^{(1)}$ for the $1.25 \times 1.25$ grid, where $\boldsymbol{W}_{Q1}^{(1)}$ denotes the first-order for spatial area-based model.

$$\mathbf{W}_{Q1}^{(1)} = \begin{bmatrix} 0 & 0 & 0 & 0.33 & 0.33 & 0.33 & \cdots & 0.33 \\ 0 & 0 & 0 & 0 & 0 & 0.25 & \cdots & 0 \\ 0 & 0 & 0 & 0.5 & 0.5 & 0 & \cdots & 0 \\ \vdots & \vdots & \vdots & \vdots & \vdots & \vdots & \ddots & \vdots \\ 0.33 & 0 & 0 & 0 & 0.33 & 0 & \cdots & 0 \end{bmatrix} \qquad \mathbf{W}_{Q2}^{(1)} = \begin{bmatrix} 0 & 1 & 0 \\ 0.5 & 0 & 0.5 \\ 0 & 1 & 0 \end{bmatrix}$$

In the spatial area-based representation, a value of 1 indicates that two sub-districts are adjacent under the Queen Contiguity rule, and 0 otherwise. As shown in Fig. 5, the sub-district highlighted in cream (Jelai Hulu) represents the observed location, while the yellow areas denote its first-order neighbours. A similar structure applies to the $1.25 \times 1.25$ grid, where the red-hatched cell (A2) serves as the observed location, with A1 and A3 identified as its neighbouring cells. This row-standardized weighting structure ensures comparability across locations with different numbers of neighbours and provides a consistent basis for estimating spatial dependencies. Accordingly, only the first-order spatial lag is incorporated into the GSTAR(1;1) model, as it sufficiently captures the dominant spatial interactions required for accurate parameter estimation.

### 3.3. Parameter Estimation and Diagnostic Test

The parameter estimation for the GSTAR(1;1) models was conducted using the Ordinary Least Squares (OLS) method with the previously defined Queen Contiguity spatial weights. Table 3 presents the results of this initial estimation, along with the diagnostic tests for the model residuals. For a model to be considered valid, its residuals must satisfy the white noise assumption, meaning they are both independent and normally distributed. Residual independence was evaluated using the Ljung–Box test with 30 lags, while residual normality was assessed qualitatively through Q–Q normal plots.

The parameter estimation results in Table 3 reveal varied values across locations. In the initial estimation (before), several parameters were found to be statistically insignificant, as indicated by the red text. Here, the term before refers to the results of the first parameter estimation, prior to the re-estimation process, while after denotes the results obtained following the re-estimation. Since insignificant parameters do not contribute meaningfully to the model's predictive ability, they were excluded to obtain a more parsimonious and stable model. Accordingly, a re-estimation process was conducted in which the insignificant parameters were set to zero (highlighted in blue) and the model was iteratively refitted until only statistically significant parameters remained. To ensure that this refinement did not introduce bias, the final model was formally evaluated using the AIC and BIC. The results confirmed that the Final (After) Model is statistically superior: the Full Model produced AIC = 8353.66 and BIC = 8485.72, whereas the Final (Pruned) Model produced substantially lower values (AIC = 8289.68 and BIC = 8336.85). This evidence validates the exclusion of insignificant parameters and confirms that the final model presented in Table 3.

**Table 3:** Parameter estimation and diagnostic test. Red and blue values represent insignificant parameters and those set to zero, respectively. "Yes" indicates that the normality and independence assumptions are satisfied, while "No" indicates that they are not.

| **Spatial Unit** | **Loc. ($i$)** | **Before** | | | | | **After** | | | | |
|---|---|---|---|---|---|---|---|---|---|---|---|
| | | **Parameter** | | **Diag.Test** | | **RMSE** | **Parameter** | | **Diag.Test** | | **RMSE** |
| | | $\phi_{10}^{(i)}$ | $\phi_{11}^{(i)}$ | **Norm.** | **Ind.** | | $\phi_{10}^{(i)}$ | $\phi_{11}^{(i)}$ | **Norm.** | **Ind.** | |
| Area | Jelai Hulu (1) | -0.02 | 0.36 | Yes | Yes | 7.42 | 0.00 | 0.34 | Yes | Yes | **7.42** |
| | Kapuas (2) | -0.06 | -0.36 | Yes | Yes | | -0.06 | -0.36 | Yes | Yes | |
| | Kendawangan (3) | -0.54 | 0.60 | Yes | Yes | | -0.54 | 0.60 | Yes | Yes | |
| | Manis Mata (4) | 0.09 | -0.10 | Yes | Yes | | 0.07 | 0.00 | Yes | Yes | |
| | Marau (5) | -0.02 | 0.01 | Yes | Yes | | 0.00 | 0.00 | Yes | Yes | |
| | Meliau (6) | 0.00 | 0.00 | Yes | Yes | | 0.00 | 0.00 | Yes | Yes | |
| | Nanga Taman (7) | -0.03 | 0.00 | Yes | Yes | | 0.00 | 0.00 | Yes | Yes | |
| | Nanga Tayap (8) | 0.01 | -0.01 | No | Yes | | 0.00 | 0.00 | Yes | Yes | |
| | Sandai (9) | 0.00 | 0.01 | Yes | Yes | | 0.00 | 0.00 | Yes | Yes | |
| | Sekadau Hilir (10) | -0.02 | 0.02 | No | Yes | | 0.00 | 0.00 | Yes | Yes | |
| | Sekadau Hulu (11) | -0.01 | -0.02 | No | Yes | | 0.00 | 0.00 | Yes | Yes | |
| | Simpang Hulu (12) | -0.05 | 0.12 | Yes | Yes | | 0.00 | 0.10 | Yes | Yes | |
| | Sungai Laur (13) | -0.02 | -0.50 | Yes | Yes | | 0.00 | -0.52 | Yes | Yes | |
| | Tumbang Titi (14) | -0.97 | -0.76 | Yes | Yes | | -0.97 | -0.76 | Yes | Yes | |
| Grid $1.25 \times 1.25$ | A1 (1) | -0.02 | 0.13 | Yes | Yes | 8.16 | 0.00 | 0.15 | Yes | Yes | 8.14 |
| | A2 (2) | -0.04 | 0.05 | Yes | Yes | | 0.00 | 0.00 | Yes | Yes | |
| | A3 (3) | -0.24 | 0.14 | Yes | Yes | | -0.24 | 0.14 | Yes | No | |

For the spatial area-based model, after the re-estimation process, the significant parameters were identified as: $\phi_{11}$ for Jelai Hulu; both $\phi_{10}$ and $\phi_{11}$ for Kapuas and Kendawangan; $\phi_{10}$ for Manis Mata; $\phi_{11}$ for Simpang Hulu and Sungai Laur; and both $\phi_{10}$ and $\phi_{11}$ for Tumbang Titi. The resulting refined model achieved a significantly improved RMSE of 7.42, and its residuals successfully met the assumptions of normality and independence. For the Grid $1.25 \times 1.25$ model, the re-estimation process yielded a final model where the significant parameters were the spatial parameter ($\phi_{11}$) for location A1, and both the temporal ($\phi_{10}$) and spatial ($\phi_{11}$) parameters for

location A3. Notably, for location A2, both parameters were found to be insignificant and were thus removed from the final model. This refined grid model produced a RMSE of 8.14, with its residuals satisfying the normality assumption but not the independence assumption.

### 3.4. Accuracy Model

A comparison of the predictive accuracy between the two final models shows that both the spatial area-based model (RMSE = 7.42, see the bolded value in Table 3) and the Grid $1.25 \times 1.25$ model (RMSE = 8.14, as shown in the RMSE column of Table 3) demonstrate strong forecasting performance. However, the spatial area-based model was selected as the final model because its residuals satisfied the white noise assumptions, whereas the Grid $1.25 \times 1.25$ model did not. Therefore, the spatial area-based model is considered the most appropriate for this study.

The final GSTAR model reveals diverse and location-specific fire dynamics across sub-districts. Jelai Hulu and Simpang Hulu are characterized by positive lagged spatial spillover effects, meaning fire risk intensifies at time $t$ when neighboring activity was high at time $t-1$. In contrast, Sungai Laur shows a negative lagged spatial spillover effect, indicating reduced local risk at time $t$ when adjacent areas experienced higher fire activity at time $t-1$. Manis Mata operates as a spatially independent system, influenced solely by its own temporal behavior, as shown by the orange-highlighted (see Eq. (1)). In Kapuas and Tumbang Titi, spatial relationships are also defined by negative lagged spatial spillover effects, whereas Kendawangan exhibits a positive lagged spatial spillover effect (reinforcement). Overall, these patterns demonstrate that fire behavior varies markedly across regions, with the model effectively capturing each sub-district's unique spatial-temporal interactions. The GSTAR(1;1) specification for the selected spatial area-based model employs the Queen Contiguity weight matrix, and the model equation can be expressed as follows:

$$
\begin{aligned}
\hat{Y}_t^{(1)} &= 0.113(Y_{t-1}^{(4)} + Y_{t-1}^{(5)} + Y_{t-1}^{(14)}) \\
\hat{Y}_t^{(2)} &= -0.062Y_{t-1}^{(2)} - 0.089(Y_{t-1}^{(6)} + Y_{t-1}^{(7)} + Y_{t-1}^{(10)} + Y_{t-1}^{(11)}) \\
\hat{Y}_t^{(4)} &= 0.071Y_{t-1}^{(4)} \\
\hat{Y}_t^{(12)} &= 0.048(Y_{t-1}^{(6)} + Y_{t-1}^{(13)}) \\
\hat{Y}_t^{(13)} &= -0.259(Y_{t-1}^{(9)} + Y_{t-1}^{(12)}) \\
\hat{Y}_t^{(14)} &= -0.973Y_{t-1}^{(14)} - 0.255(Y_{t-1}^{(1)} + Y_{t-1}^{(5)} + Y_{t-1}^{(8)})
\end{aligned}
\tag{1}
$$

To evaluate the performance of the selected spatial area-based GSTAR model, Fig. 6 presents a visual comparison between the actual observed FRP values and the model's predictions for four representative sub-districts, illustrating the performance of the GSTAR(1;1) model by comparing the actual FRP values (green line) with in-sample predictions (blue line) and out-of-sample forecasts (yellow line). Overall, the in-sample predictions closely follow the observed FRP trends, capturing the main peaks during high-fire periods in August–September 2024 and July–August 2025. In Jelai Hulu (Fig. 6a) and Kapuas (Fig. 6b), the in-sample estimates successfully reproduce the major historical peaks observed in the data, particularly during the early dry-season spikes and the prominent August events. The out-of-sample forecasts for September capture the general upward movement but appear smoother than the actual values, indicating that the model tends to moderate short-term volatility. In Kendawangan (Fig. 6c), the in-sample forecasts generally follow the overall pattern of the observed data, including the fluctuations during periods of increased fire activity. The out-of-sample predictions for September also capture the upward movement, although some deviations in magnitude remain. For Manis Mata (Fig. 6d), the model adequately reproduces the major historical spikes in the in-sample period and successfully indicates the renewed increase in fire activity during the out-of-sample weeks, even though the predicted values are smoother than the observed series. Despite minor discrepancies and a

tendency to smooth sudden extreme spikes, the GSTAR model effectively captures temporal dynamics and periodic fire behavior in West Kalimantan.

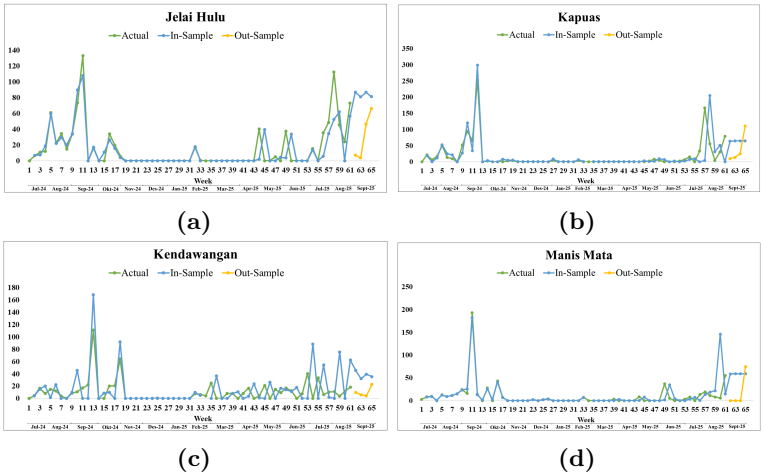


**Fig. 6:** Comparison of Actual Data (green line), In-Sample Fit (blue line), and Out-of-Sample (yellow line) forecast for four representative sub-districts: (a) Jelai Hulu, (b) Kapuas, (c) Kendawangan, and (d) Manis Mata

Consequently, the forecasts produced by the model are subsequently used for spatial interpolation via the Ordinary Kriging method, as reported in Table 4.

**Table 4:** FRP prediction and 95% prediction intervals for October. Yellow numbers represent locations ($i$).

| Regencies | Subdistrict ($i$) | Week 1 | Intervals | Week 2 | Intervals | Week 3 | Intervals | Week 4 | Intervals | Illustration |
|---|---|---|---|---|---|---|---|---|---|---|
| Sanggau | Kapuas (2) | 98.44 | (82.25 – 114.62) | 98.06 | (81.87 – 114.25) | 98.05 | (81.86 – 114.24) | 98.05 | (81.86 – 114.24) | 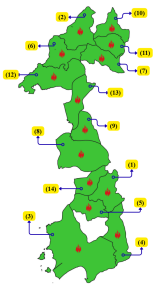 |
| | Meliau (6) | 58.15 | (58.15 – 58.15) | 58.15 | (58.15 – 58.15) | 58.15 | (58.15 – 58.15) | 58.15 | (58.15 – 58.15) | |
| Sekadau | Sekadau Hilir (10) | 111.17 | (111.17 – 111.17) | 111.17 | (111.17 – 111.17) | 111.17 | (111.17 – 111.17) | 111.17 | (111.17 – 111.17) | |
| | Sekadau Hulu (11) | 55.39 | (55.39 – 55.39) | 55.39 | (55.39 – 55.39) | 55.39 | (55.39 – 55.39) | 55.39 | (55.39 – 55.39) | |
| | Nanga Taman (7) | 80.15 | (80.15 – 80.15) | 80.15 | (80.15 – 80.15) | 80.15 | (80.15 – 80.15) | 80.15 | (80.15 – 80.15) | |
| Ketapang | Jelai Hulu (1) | 83.83 | (75.93 – 91.74) | 84.50 | (76.52 – 92.47) | 84.52 | (76.53 – 92.52) | 84.51 | (76.51 – 92.51) | |
| | Nanga Tayap (8) | 68.43 | (68.43 – 68.43) | 68.43 | (68.43 – 68.43) | 68.43 | (68.43 – 68.43) | 68.43 | (68.43 – 68.43) | |
| | Sandai (9) | 64.11 | (64.11 – 64.11) | 64.11 | (64.11 – 64.11) | 64.11 | (64.11 – 64.11) | 64.11 | (64.11 – 64.11) | |
| | Kendawangan (3) | 64.86 | (47.71 – 82.01) | 68.68 | (51.40 – 85.96) | 69.05 | (51.76 – 86.33) | 69.08 | (51.80 – 86.37) | |
| | Sungai Laur (13) | 131.65 | (129.01 – 134.29) | 131.59 | (128.95 – 134.23) | 131.59 | (128.95 – 134.23) | 131.59 | (128.95 – 134.23) | |
| | Simpang Hulu (12) | 133.26 | (129.48 – 137.03) | 133.19 | (129.41 – 136.97) | 133.19 | (129.41 – 136.97) | 133.19 | (129.41 – 136.97) | |
| | Marau (5) | 173.68 | (173.68 – 173.68) | 173.68 | (173.68 – 173.68) | 173.68 | (173.68 – 173.68) | 173.68 | (173.68 – 173.68) | |
| | Manis Mata (4) | 82.45 | (74.79 – 90.11) | 83.29 | (75.59 – 91.00) | 83.38 | (75.68 – 91.09) | 83.39 | (75.69 – 91.10) | |
| | Tumbang Titi (14) | 86.37 | (68.92 – 103.83) | 85.97 | (66.21 – 105.73) | 85.67 | (65.36 – 105.98) | 85.51 | (65.06 – 105.96) | |

*Note: All FRP values are expressed in Megawatts (MW).*

## 3.5. Interpolation of Fire Radiative Power (FRP)

Before performing spatial interpolation, the forecasted FRP data were first evaluated to ensure compliance with the Kriging model assumptions. A visual inspection confirmed mean stationarity, and the Augmented Dickey-Fuller (ADF) test was also performed on the spatial residuals, yielding $p$-values consistently above 0.05. This formal testing, despite its result, was mitigated by the fact that the spatial trend had already been explicitly removed using linear regression (FRP $\sim x + y$) prior to Kriging. Meanwhile, the Kolmogorov–Smirnov test indicated non-normality. Consequently, a logarithmic transformation was applied, successfully normalizing the data for geostatistical analysis. Subsequently, the spatial dependence structure was modeled using a semivariogram. The model selection process was based on the lowest Root Mean Square Error (RMSE) values, representing the best fit and highest estimation accuracy. The comparison of semivariogram models for each week is presented in Fig. 7, which shows that all variogram models yielded the same RMSE value of 0.08 across the four weeks.

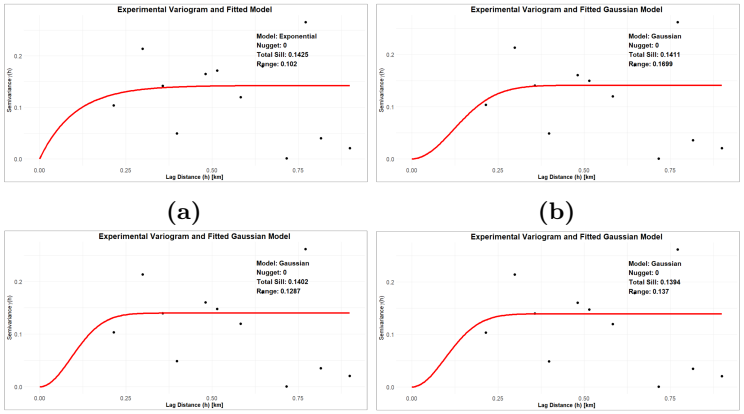


**(a)** **(b)** **(c)** **(d)**

**Fig. 7:** Semivariogram model plots with RMSE value of 0.08 for each week: (a) Week 1 Exponential model, (b) Week 2 Gaussian model, (c) Week 3 Gaussian model, and (d) Week 4 Gaussian model.

Therefore, spatial interpolation using Ordinary Kriging was conducted based on these models, and the resulting prediction maps are presented in Fig. 8.

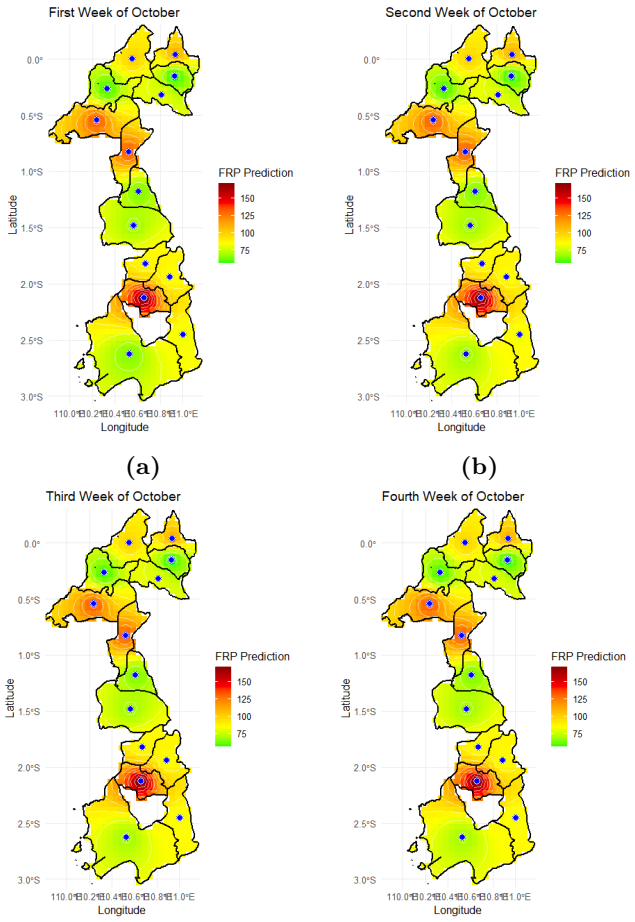


**(a)** **(b)** **(c)** **(d)**

**Fig. 8:** Interpolated FRP forecast maps for October 2025 (a) first week, (b) second week, (c) third week, and (d) fourth week

The interpolated forecast maps for October indicate that there are no significant changes in spatial fire intensity patterns from the first to the fourth week. Overall, the predicted FRP distribution remains relatively stable throughout the month. However, in the fourth week, a slight decrease in FRP levels is observed in the Nanga Tayap and Sandai sub-districts, as reflected

by the color transition from light green to a darker green shade (see Fig. 8d). This subtle shift suggests a localized reduction in fire potential, while the general spatial configuration of fire activity remains consistent across the observed period. A comparative illustration of the initial map, the GSTAR forecast map, and the Kriging interpolation results can be seen in Fig. 9.

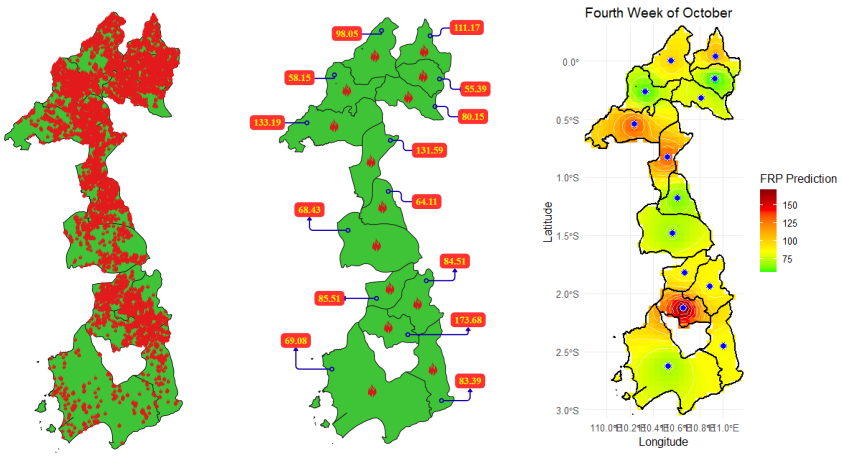


**(a)** **(b)** **(c)**

**Fig. 9:** Comparison of spatial patterns: (a) actual FRP distribution, (b) Ilustration of GSTAR(1;1) model prediction, and (c) interpolated prediction using Ordinary Kriging.

## 4. Conclusion

This study successfully applied the GSTAR(1;1) and Ordinary Kriging methods to predict and visualize the spatial distribution of Fire Radiative Power (FRP) in Sanggau, Sekadau, and Ketapang Regencies. Using a spatial area-based approach, the model achieved optimal performance with a RMSE value of 7.42 and residuals that satisfied the white noise assumption, indicating good forecasting reliability. The prediction results for October 2025 show that the spatial fire intensity patterns remained relatively stable from the first to the fourth week. A minor decrease in FRP levels was observed in the Nanga Tayap and Sandai sub-districts during the final week, reflecting localized improvements in fire conditions. Overall, the integrated GSTAR–Kriging approach effectively captured both temporal and spatial patterns of FRP, making it a valuable tool for monitoring and managing fire risk in West Kalimantan. Furthermore, this integrated framework can support regional decision-making for wildfire management and environmental protection, providing a robust basis for preventive and mitigation strategies in fire-prone areas.

## CRediT Authorship Contribution Statement

**Gita Fitriyana:** Conceptualization, Methodology, Writing-Original Draft. **Nurfitri Imro'ah:** Data Curation, Formal Analysis, Writing–Review & Editing. **Nur'ainul Miftahul Huda:** Data Curation, Formal Analysis, Writing–Review & Editing.

## Declaration of Generative AI and AI-assisted technologies

No generative AI or AI-assisted technologies were used during the preparation of this manuscript.

## Declaration of Competing Interest

The authors declare no competing interests.

## Funding and Acknowledgments

This research received no external funding.

## Data and Code Availability

The data and code supporting the findings of this study are available from the corresponding author upon reasonable request and subject to confidentiality agreements.

## References


[1] Carolina Filizzola et al. "Fire Characterization by Using an Original RST-Based Approach for Fire Radiative Power (FRP) Computation". In: *Fire* 6.2 (2023), p. 48. DOI: 10.3390/fire6020048.

[2] Gita Fitriyana et al. "Interpolation of Fire Radiative Power in West Kalimantan using Ordinary Kriging". In: *Jurnal Teori dan Aplikasi Matematika* 9.4 (2025), pp. 1287–1300. DOI: 10.31764/jtam.v9i4.32643.

[3] Elizabeth B. Wiggins et al. "High Temporal Resolution Satellite Observations of Fire Radiative Power Reveal Link Between Fire Behavior and Aerosol and Gas Emissions". In: *Geophysical Research Letters* 47.23 (2020). DOI: 10.1029/2020gl090707.

[4] Sanath Sathyachandran Kumar et al. "Potential Underestimation of Satellite Fire Radiative Power Retrievals over Gas Flares and Wildland Fires". In: *Remote Sensing* 12.2 (2020), p. 238.

[5] Zixun Dong et al. "A Deep Learning Framework: Predicting Fire Radiative Power From the Combination of Polar-Orbiting and Geostationary Satellite Data During Wildfire Spread". In: *IEEE Journal of Selected Topics in Applied Earth Observations and Remote Sensing* 17 (2024), pp. 10827–10841. DOI: 10.1109/jstars.2024.3403146.

[6] Hesty Pratiwi, Nurfitri Imro'ah, and Nur'ainul Miftahul Huda. "FOREST FIRE ANALYSIS FROM PERSPECTIVE OF SPATIAL-TEMPORAL USING GSTAR (p;$\lambda_1$, $\lambda_2$, ..., $\lambda_p$) MODEL". In: *BAREKENG: Jurnal Ilmu Matematika dan Terapan* 19.2 (2025), pp. 1379–1392. DOI: 10.30598/barekengvol19iss2pp1379-1392.

[7] Y. Supriya and Thippa Reddy Gadekallu. "Particle Swarm-Based Federated Learning Approach for Early Detection of Forest Fires". In: *Sustainability* 15.2 (2023), p. 964. DOI: 10.3390/su15020964.

[8] Ramez Alkhatib et al. "A Brief Review of Machine Learning Algorithms in Forest Fires Science". In: *Applied Sciences* 13.14 (2023), p. 8275. DOI: 10.3390/app13148275.

[9] Muhammad Yahya Ayyash, Nur'ainul Miftahul Huda, and Nurfitri Imro'ah. "The GSTAR (1;1) Modelling with Three Combination of the Grid Sizes and Spatial Weight Matrix in Forest Fires Cases". In: *JTAM (Jurnal Teori dan Aplikasi Matematika)* 9.1 (2025), p. 134. DOI: 10.31764/jtam.v9i1.27543.

[10] Xiao Lu et al. "Stochastic Geometry Analysis of Spatial-Temporal Performance in Wireless Networks: A Tutorial". In: *IEEE Communications Surveys & Tutorials* 23.4 (2021), pp. 2753–2801. DOI: 10.1109/comst.2021.3104581.

[11] Sang Yong Chung et al. "Supplement of Missing Data in Groundwater-Level Variations of Peak Type Using Geostatistical Methods". In: *GIS and Geostatistical Techniques for Groundwater Science*. Elsevier, 2019, pp. 33–41. DOI: 10.1016/b978-0-12-815413-7.00004-3.

[12] Utriweni Mukhaiyar et al. "Prediksi Risiko Emisi Karbon Dioksida Melalui Pemodelan GSTAR Kriging di Wilayah Asia". In: *Journal of Mathematics, Computations and Statistics* 7.2 (2024), pp. 396–412. DOI: 10.35580/jmathcos.v7i2.4309.

[13] Jyoti U. Devkota. "Statistical analysis of active fire remote sensing data: examples from South Asia". In: *Environmental Monitoring and Assessment* 193.9 (2021). DOI: 10.1007/s10661-021-09354-x.

[14] Nur'ainul Miftahul Huda et al. "Forest Fires in Peatlands Analyzed from Various Perspectives: Spatial, Temporal, and Spatial-Temporal". In: *JTAM (Jurnal Teori dan Aplikasi Matematika)* 9.2 (2025), p. 482. DOI: 10.31764/jtam.v9i2.28884.

[15] Feby Hestuningtias and Muhammad Hasan Sidiq Kurniawan. "The Implementation of the Generalized Space-Time Autoregressive (GSTAR) Model for Inflation Prediction". In: *Enthusiastic: International Journal of Applied Statistics and Data Science* (2023), pp. 176–188. DOI: 10.20885/enthusiastic.vol3.iss2.art5.

[16] Hesty Pratiwi et al. "Comparison of weight matrix in hotspot modeling in West Kalimantan using the GSTAR method". In: *Jurnal Matematika UNAND* 14.1 (2025), pp. 31–45. DOI: 10.25077/jmua.14.1.31-45.2025.

[17] Yundari et al. "Spatial Weight Determination of GSTAR(1;1) Model by Using Kernel Function". In: *Journal of Physics: Conference Series* 1028 (2018), p. 012223. DOI: 10.1088/1742-6596/1028/1/012223.

[18] Nur'ainul Miftahul Huda and Nurfitri Imro'ah. "Determination of the best weight matrix for the Generalized Space Time Autoregressive (GSTAR) model in the Covid-19 case on Java Island, Indonesia". In: *Spatial Statistics* 54 (2023), p. 100734. DOI: 10.1016/j.spasta.2023.100734.

[19] Yundari Yundari, Udjianna Sekteria Pasaribu, and Utriweni Mukhaiyar. "Error Assumptions on Generalized STAR Model". In: *Journal of Mathematical and Fundamental Sciences* 49.2 (2017), p. 136. DOI: 10.5614/j.math.fund.sci.2017.49.2.4.

[20] Pramod Kumar et al. "Spatial variation of permeability and consolidation behaviors of soil using ordinary kriging method". In: *Groundwater for Sustainable Development* 20 (2023), p. 100856. DOI: 10.1016/j.gsd.2022.100856.

[21] Changshan Wu. *Interpolation: Kriging*. 2017. DOI: 10.1002/9781118786352.wbieg0996.

[22] Jürgen Böhner and Benjamin Bechtel. "GIS in Climatology and Meteorology". In: *Comprehensive Geographic Information Systems*. Elsevier, 2018, pp. 196–235. DOI: 10.1016/b978-0-12-409548-9.09633-0.

[23] Novia Nur Rohma. "Estimation of Ordinary Kriging Method with Jackknife Technique on Rainfall Data in Malang Raya". In: *International Journal on Information and Communication Technology (IJoICT)* 8.2 (2022), pp. 22–39. DOI: 10.21108/ijoict.v8i2.678.

[24] Mohsin Khan et al. "Spatial interpolation of water quality index based on Ordinary kriging and Universal kriging". In: *Geomatics, Natural Hazards and Risk* 14.1 (2023). DOI: 10.1080/19475705.2023.2190853.

[25] Tung Gia Pham et al. "Application of Ordinary Kriging and Regression Kriging Method for Soil Properties Mapping in Hilly Region of Central Vietnam". In: *ISPRS International Journal of Geo-Information* 8.3 (2019), p. 147. DOI: 10.3390/ijgi8030147.

[26] Meng Li et al. "Kriging-based reliability analysis considering predictive uncertainty reduction". In: *Structural and Multidisciplinary Optimization* 63.6 (2021), pp. 2721–2737. DOI: 10.1007/s00158-020-02831-w.

[27] Andie Setiyoko, T. Basaruddin, and Aniati Murni Arymurthy. "Minimax Approach for Semivariogram Fitting in Ordinary Kriging". In: *IEEE Access* 8 (2020), pp. 82054–82065. DOI: 10.1109/access.2020.2991428.

[28] Haiyang Xia et al. "Radio environment map construction by adaptive ordinary Kriging algorithm based on affinity propagation clustering". In: *International Journal of Distributed Sensor Networks* 16.5 (2020), p. 155014772092248. DOI: 10.1177/1550147720922484.

[29] Andy H. Wong and Tae J. Kwon. "Development and Evaluation of Geostatistical Methods for Estimating Weather Related Collisions: A Large-Scale Case Study". In: *Transportation Research Record: Journal of the Transportation Research Board* 2675.11 (2021), pp. 828–840. DOI: 10.1177/03611981211020008.

[30] NASA Scientific Visualization Studio. *Active Fires As Observed by VIIRS, 2020*. Accessed on October 31, 2025. NASA Goddard Space Flight Center. 2021. https://svs.gsfc.nasa.gov/4899.

[31] Utriweni Mukhaiyar. "The goodness of generalized STAR in spatial dependency observations modeling". In: *AIP Conference Proceedings*. AIP Publishing LLC, 2015. DOI: 10.1063/1.4936436.

[32] Afnita Roza, Evony Silvino Violita, and Sherly Aktivani. "Study of Inflation using Stationary Test with Augmented Dickey Fuller & Phillips-Peron Unit Root Test (Case in Bukittinggi City Inflation for 2014-2019)". In: *EKSAKTA: Berkala Ilmiah Bidang MIPA* 23.02 (2022), pp. 106–116. DOI: 10.24036/eksakta/vol23-iss02/303.